DESIGN OF A LARGE RANGE XY NANOPOSITIONING SYSTEM

Shorya Awtar* and Gaurav Parmar
Precision Systems Design Laboratory
Mechanical Engineering, University of Michigan
Ann Arbor MI 48109

ABSTRACT

Achieving large motion range (> 1mm) along with nanometric motion quality (< 10nm), simultaneously, has been a key challenge in nanopositioning systems. Practical limitations associated with the individual physical components (bearing, actuators, and sensors) and their integration, particularly in the case of multi-axis systems, have restricted the range of currently available nanopositioning systems to approximately 100μm per axis. This paper presents a novel physical system layout, comprising a bearing, actuators, and sensors, that enables large range XY nanopositioning. The bearing is based on a parallel-kinematic XY flexure mechanism that provides a high degree of geometric decoupling between the two motion axes by avoiding geometric over-constraint, provides actuator isolation that allows the use of large-stroke single-axis actuators, and enables a complementary end-point sensing scheme using commonly available sensors. These attributes help achieve 10mm × 10mm motion range in the proposed nanopositioning system. Having overcome the physical system design challenges, a dynamic model of proposed nanopositioning system is created and verified via system identification. In particular, dynamic nonlinearities associated with the large displacements of the flexure mechanism and resulting controls challenges are identified. The physical system is fabricated, assembled, and tested to validate its simultaneous large range and nanometric motion capabilities. Preliminary closed-loop test results, which highlight the potential as well as pending challenges associated with this new design configuration, are presented.

1. INTRODUCTION

A nanopositioning system is a mechatronic motion system capable of nanometric motion quality, which is defined in terms of precision (motion repeatability), accuracy (lack of error), and resolution (minimum incremental motion) [1-5]. It comprises a bearing, actuators and drivers, sensors and electronics, and feedback controls implemented on a microcontroller.

Given their high motion quality, nanopositioning systems are vital to several existing and emerging nano-scale microscopy, manipulation, and manufacturing methods [3, 4]. Existing flexure-based nanopositioning systems are generally capable of providing approximately 100μm motion range per axis [6-10]. However, there is now a growing need for XY nanopositioning systems that can provide motion range of several millimeters while maintaining nanometric quality in a compact desktop-size package. Such applications include scanning probe microscopy and metrology [11-15], scanning probe nanolithography [16, 17], memory storage [18], hard-drive [19] and semiconductor inspection [20], semiconductor packaging [21], and biological imaging [22].

Nanopositioning systems predominantly employ non-contact bearings to avoid friction and backlash. Presence of these non-deterministic effects otherwise make feedback control design particularly difficult and restrict the motion quality to hundreds of nanometers [23, 24]. While mag-lev [25, 26] and aerostatic bearings [27, 28], are able to provide large range and high precision, owing to their non-contact operation, flexure bearings offer unmatched simplicity in design and operation, and are therefore the most common bearing choice for desktop-size nanopositioning systems [4-9, 29]. Their monolithic (joint-less) construction entirely eliminates friction and backlash leading to sub-nanometric precision, zero maintenance, and potentially infinite life. However, the main limitation of flexure bearings has been their small range of motion, which in turn has restricted the range of flexure-based nanopositioning systems.

The most common approach to overcome this range limitation is to mount a 'fine' flexure-based nanopositioning system on top of a 'coarse' large-range traditional motion system [13, 14, 20, 22, 30, 31]. While advanced design and control methods have demonstrated steady state nanometric precision and resolution in point-to-point positioning in such systems, tracking dynamic command profiles with nanometric motion quality is still an unmet challenge [32]. Moreover, this arrangement makes the system more complex, bulky, and expensive due to additional physical components.

A desired motion range of ~10mm while maintaining a motion quality ~1nm represents a dynamic range of 10^7, which poses challenge in terms of each of the individual physical components of a flexure-based nanopositioning system. Further design challenges arise from the integration of these physical components, especially in the case of multi-axis systems. Our objective in this paper is to overcome these physical system design challenges and set the stage for control system design, as the first step in achieving large range nanopositioning.

We outline the physical challenges associated with components and system integration in Section 2, and present a physical system concept for a large range parallel-kinematic XY nanopositioning system that overcomes these challenges in Section 3. Design of experimental hardware, fabrication and assembly, and component specification are covered in Section 4. Section 5 presents a lumped-parameter dynamic model of the

---

1

proposed overall system and its validation via experimental system identification. Section 6 discusses the challenges in controlling this system to meet the various closed-loop dynamic performance requirements, along with our preliminary attempts to address some of these. Open- and closed-loop testing presented in Section 7 confirms the feasibility of 10mm × 10mm motion range along with nanometric motion quality but also highlights remaining challenges.

2. CHALLENGES IN ACHIEVING LARGE RANGE

Multi-axis nanopositioning systems may be conceived in either a serial [33-35] or parallel [29, 36, 37] kinematic configuration. An XY serial kinematic configuration is simply comprised of two orthogonally arranged single-axis stages, one stacked on top of the other, resulting in an obvious but bulky construction. An XY parallel kinematic configuration is one in which both the X and Y actuators are ground-mounted, which yields a compact layout. This generally results in higher bandwidth due to the lack of moving actuators and greater precision due to the lack of disturbance from moving cables.

Despite these benefits, parallel kinematic configurations are non-obvious in their conception and often exhibit over-constraint. Over-constraint arises from a geometric layout that exhibits coupling between the two motion axes, which ultimately leads to binding and restricts motion range. Systematic constraint-based methods for the conception of XY parallel-kinematic flexure mechanisms that avoid such over-constraint have been reported previously [38, 39]. However, to achieve large range, the design of the nanopositioning system has to incorporate the flexure bearing along with the actuators and sensors from the very conception stage. The former cannot be designed in isolation, with actuators and sensors being an after-thought. The individual physical attributes and limitations of these components, described in the following paragraphs, strongly influence large-range nanopositioning capability.

The actuator itself has to be capable of large range and nanometric motion quality to meet the desired objective. This generally implies the use of direct-drive large-stroke linear actuators that are free of any friction and backlash. One of the most important attributes of such linear actuators is that they generate motion along an 'actuation axis', defined by their geometry, and do not tolerate off-axis loads or displacements. For example, electromagnetic actuators (voice coils and linear motors), which are capable of large range and high motion quality, have to be guided along its actuation axis to ensure uniform actuation force. Piezo-electric actuators, e.g. Lead Zirconate Tintanate (PZT) ceramic stacks, provide high motion quality and may be used in conjunction with displacement amplifiers in large-range nanopositioning. However, any loads acting in directions other than the axis of the brittle ceramic stack cause permanent damage to the actuator. Quasi-static and ultrasonic piezomotors, which provide incremental stepping motion (~ 10nm step size) over large travel ranges (~ 100mm), are also common in large range nanopositioning applications [13, 40, 41]. But once again their motion is strictly guided along a specified actuation axis.

Sensing requirements for large-range multi-axis nanopositioning are equally challenging. Given the stringent motion quality requirements, end-point sensing of the moving stage displacements with respect to the reference ground is indispensable. Moreover, multi-axis (XY) motion requires that the sensor for one axis be tolerant of displacements along the other axis. However, most sensors that provide large measurement range and nanometric resolution, e.g. Linear Variable Differential Transducers (LVDT) and linear optical encoders, also have a fixed 'sensing axis' defined by their geometry. These sensors are restricted to measurements along the sensing axis only and are intolerant to any off-axis motion deviations [42]. Capacitance probes, which are capable of nanometric motion quality, are unique in their ability to tolerate large off-axis displacements, making them highly suitable for multi-axis nanopositioning system. However, their measurement range is typically limited to 10-100μm, making them inadequate for large range nanopositioning. Two-axis (XY) optical gratings can provide end-point sensing and large range, while circumventing the off-axis tolerance issue; however, currently available products do not provide a high enough accuracy [43]. Finally, even though laser interferometry can provide large range, along with nanometric resolution, repeatability and accuracy, and tolerance to off-axis displacements, its use in desktop applications has traditionally been limited by its size and set-up complexity. While miniature versions that make use of fiber-optic cables have become available more recently, their integration within a nanopositioning system remains a challenge [44].

The lack of system-level conceptualization – that considers the flexure bearing, actuator, and sensor in conjunction, and accommodates the limitations of each of these components – is the key reason why large-range nanopositioning has not been accomplished so far. Once a physical system layout that, in principle, is capable of large range and nanometric motion quality has been conceived, control system design to meet specific closed-loop performance can be carried out. We therefore proceed to compile the relevant motion requirements as well as the sensor and actuator limitations that need to be considered in a parallel-kinematic flexure-based XY nanopositioning physical system layout:

I. The two motion axes (X & Y) must be sufficiently decoupled from each other so that motion in one axis does not constrain motion in the other axis.

II. Parasitic errors along the un-actuated directions (i.e., Z, θ_x, θ_y, and θ_z) should be inherently restricted and minimized via the flexure mechanism design.

III. For each motion axis, the point of actuation on the flexure bearing should move only along the direction of actuation to accommodate the pre-defined actuation axis of large-stroke linear actuators.

IV. The layout should be such that the high-resolution large-range multi-axis end-point sensing requirement can be resolved into simpler sensing tasks that are physically realizable using existing high resolution sensors that either provides large range or tolerance to off-axis motions.

2

3. PROPOSED PHYSICAL SYSTEM DESIGN

To create physical system layouts that overcome the above-listed challenges, we propose a deterministic constraint map (Fig. 1) that systematically captures the above desired attributes in a simple graphical manner. This constraint map comprises rigid stages, interconnected by constraint elements, along with sensors and actuators. This provides the basis for generating large-range parallel-kinematic XY nanopositioning physical system layouts. Constraint-based design of XY flexure mechanisms has be reported previously [38, 39, 45]. Here we provide an overview, with particular emphasis on sensor and actuator integration.

The constraint map comprises a Motion Stage that is required to have X and Y motions with respect to a Ground. Stage 1 is connected to Ground via Constraint (A), which only allows relative X motion, so as to provide an interface with a ground-mounted large-stroke fixed-axis X direction linear actuator (e.g. linear motor, voice coil, PZT with motion amplifier, inchworm actuator). To ensure that the X displacement of Stage 1, generated by the X actuator, is transmitted to the Motion Stage while keeping the latter free to also move in the Y direction, Stage 1 and Motion Stage are connected via Constraint (C), which only allows relative Y translation between the two. An analogous arrangement is repeated along the Y direction. Stage 2 is constrained to move only in the Y direction with respect to Ground due to Constraint (B), and addresses the challenge of integrating a large-stroke Y direction linear actuator. Further, to transmit this Y motion to the Motion Stage, without affecting or being affected by the latter's X motion, Stage 2 is connected to the Motion Stage via constraint (D), which only allows relative X motion.

Assuming that the constraint elements (A), (B), (C), and (D) are ideal, i.e. they allow relative displacements only in the direction indicated by their respective double-sided arrow shown in Fig. 1, it may be readily seen that the proposed constraint map can help overcome the physical system layout challenges listed earlier. Since the X and Y motions of the Motion Stage in this parallel-kinematic arrangement are entirely decoupled, large motions along each direction are made possible by eliminating the possibility of geometric over-constraint. Given the constraint properties of the constraint elements, error motion such as in-plane yaw (θ_z) and the three out-of-plane displacements (Z, θ_x, and θ_y) are ideally zero and very small in practice.

In addition to enabling X actuator integration, Stage 1 also provides an ideal location for mounting a high-resolution, large-stroke, fixed-axis X direction primary sensor (e.g. linear encoder, LVDT) with respect to Ground. Ideally, the X displacement of the Stage 1 should be the same as that of the Motion Stage, due to constraint (C). However, in a real implementation, some small relative X displacement between the Motion Stage and Stage 1 can be expected. This displacement is measured via a second high-resolution X direction sensor. While the measurement range required of this second sensor is very small, it should be tolerant to the large relative Y displacement that occurs between Stage 1 and the
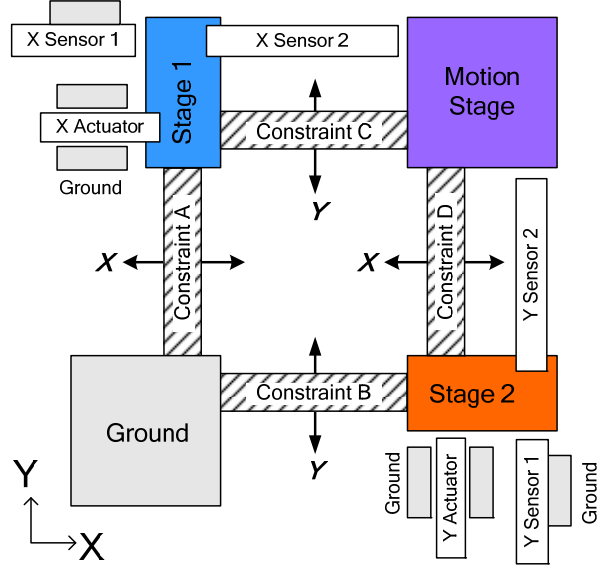

Fig. 1 Proposed Constraint Map

Motion Stage. Capacitance probes easily meet these requirements. Thus, the proposed constraint map enables large-range high-resolution multi-axis end-point sensing by resolving it into two simpler and practically realizable measurements that are simply added. A similar dual-sensor arrangement is repeated along the Y direction.

A practical realization of the proposed constraint map employing the double parallelogram flexure module as constraints (A), (B), (C), and (D), leads to the XY parallel-kinematic physical system shown in Fig. 2. A geometric mirroring, which adds Stages 3 and 4 as well as constraints (A'), (B'), (C'), and (D') to the physical layout, has been carried out without compromising the above arguments. This symmetry helps make the physical system more tolerant to manufacturing errors and thermal fluctuations. The pros and cons of the double parallelogram flexure module as a single- Degree of Freedom (DoF) constraint element and the suitability of the particular embodiment of Fig. 2 over other candidates are discussed in [45, 46]. Sensors and actuators have been intentionally omitted in these illustrations for the sake of clarity.

If the constraint elements are assumed ideal, then it is evident that an X actuation at Stage 1 produces only an X displacement of Stage 1, Stage 3 and the Motion Stage, without perturbing Stages 2 and 4 (Fig. 2A). Similarly, a Y actuation at Stage 2 produces only a Y displacement of Stage 2, Stage 4 and the Motion Stage, without perturbing Stages 1 and 3 (Fig. 2B). When the X and Y forces are applied simultaneously (Fig. 2C), X displacements only are produced at Stages 1 and 3; Y displacements only are produced at Stages 2 and 4; and the Motion Stage exhibits both X and Y displacements. The independence between the two axes of actuation, which is a consequence of the constraint layout and design symmetry, ensures large unconstrained motions along both axes. Furthermore, since all the double parallelogram flexure modules offer high stiffness in the in-plane yaw and out-of-
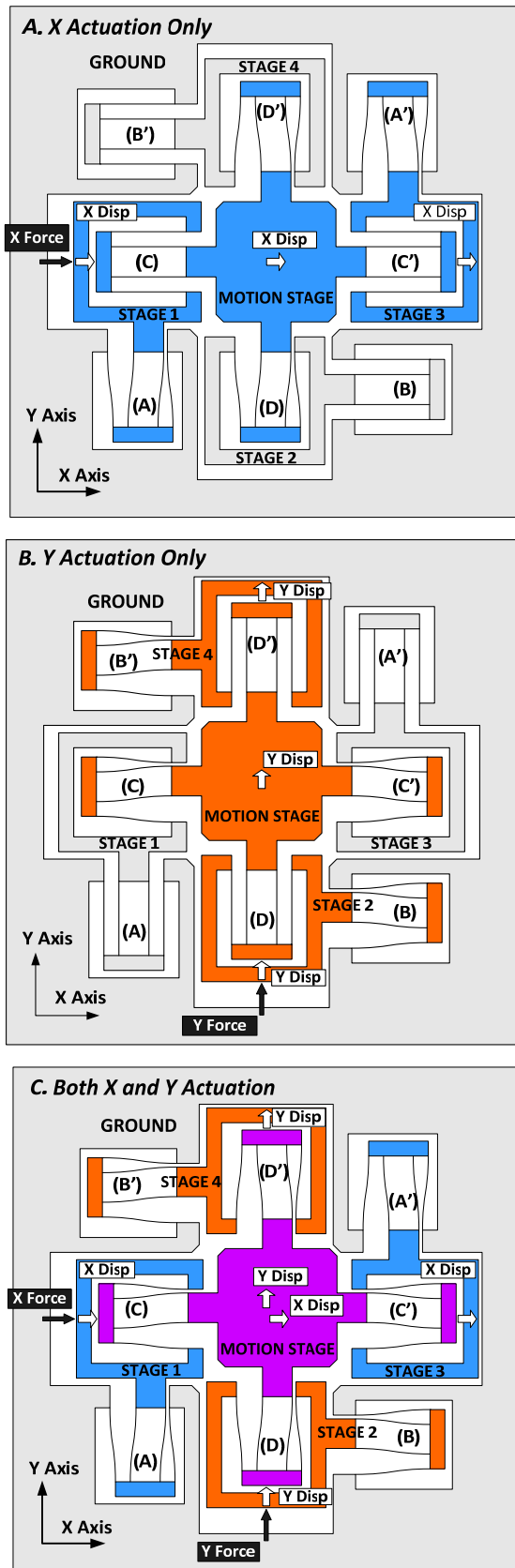
Fig. 2 Physical System Schematic

plane directions, parasitic error motions are minimized. Minor deviations from these ideal attributes are to be expected in practice, since the double parallelogram flexure modules are not perfectly ideal constraint elements.

The ease of integration of large-stroke fixed-axis linear actuators at Stage 1 and Stage 2 is as expected. Also, it is obvious that a first X sensor (large-range, fixed-axis) can measure the X displacement of Stage 1 w.r.t. Ground, while a second X sensor (small-range, axis-free) can measure X displacement of the Motion Stage w.r.t. Stage 1. Y direction sensing can also be addressed in a similar fashion. An animation of this physical system concept may be viewed at the authors' website [47].

4. EXPERIMENTAL DESIGN, FABRICATION AND ASSEMBLY

Using previously developed closed-form nonlinear parametric static analysis [38, 45], a detailed design of the XY parallel-kinematic physical system described in the previous section was carried out to achieve a target motion range of 10mm × 10mm. The hardware that was subsequently fabricated and assembled for experimental testing is illustrated in Fig. 3.

The detailed design process included **A**. the determination of all relevant dimensions of the flexure bearing, **B**. materials and manufacturing method selection, **C**. actuator, driver, sensor, and control hardware specification, and **D**. ensuring that the entire assembly is free of friction and backlash.

Flexure Bearing: The flexure bearing was sized to minimize in-plane and out-of-plane parasitic error motions as well as
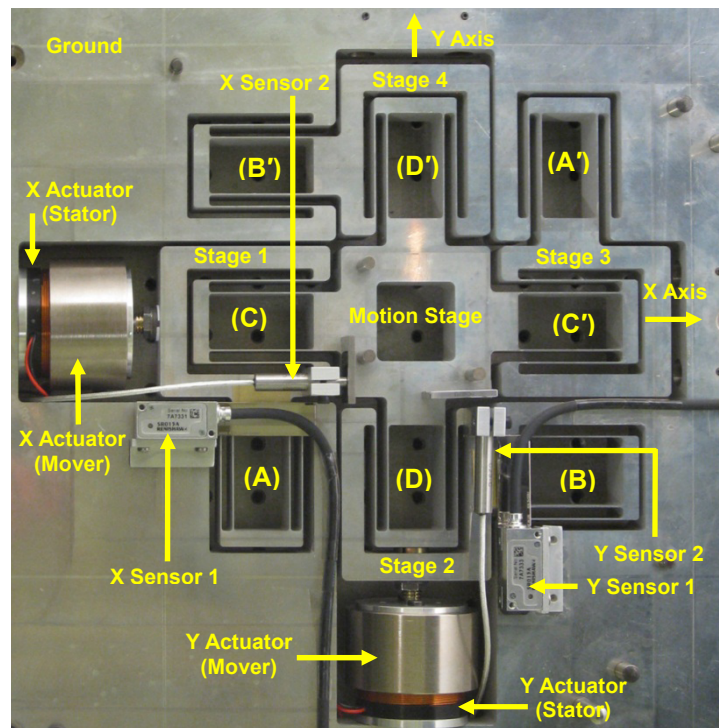

Fig.3 Proposed Large Range XY Nanopositioning System: Proof-of-Concept Prototype

4

cross-axis coupling between the X and Y directions over the motion range of interest. The resulting dimensions are as follows: center-to-center distance between adjacent double parallelogram flexure modules (DPFM) is 46.25mm; beam length is 47.5mm; beam in-plane thickness is 0.63mm, beam out-of-plane height is 25mm; and, inner and outer beam spacing in each DPFM are 12.81mm and 18.44mm, respectively. The flexure bearing along with the ground frame that is used for mounting all sensors and actuators was created monolithically from a 25.4mm thick AL6061-T651 plate, machined down to 25mm, using wire- Electric Discharge Machining (EDM). The flexure bearing spans a 255mm × 255mm area in the center, while the outer dimensions of the ground frame (and therefore the overall system) are 385mm × 385mm.

AL6061-T651 was selected as the flexure bearing material because of its good strength-to-modulus ratio, lack of cold-working stresses, long term phase stability, low cost, and ease of availability [38]. Its only drawback is a relatively high coefficient of thermal expansion (CTE), which is mitigated by the geometric symmetry of the overall layout and the individual DPFMs and therefore deemed acceptable for a proof-of-concept prototype. Wire-EDM is the only practical manufacturing method that produces straight walls over a 25mm plate height to yield thin beams and tight tolerances (± 0.005mm for the most sensitive dimensions).

The motion characteristics of the flexure bearing by itself were first measured to validate the physical arguments made in the previous section and the closed-form analytical predictions. A 10mm × 10mm motion range capability was demonstrated, along with a cross-axis coupling < 60μm, parasitic in-plane rotations < 100μrad, and out-of-plane parasitic motions < 4μm. These quasi-static error motion measurements were found to agree with analytically predicted values within 5-10%, as reported previously [45]. Having characterized and validated the flexure bearing performance, we next present the selection of the actuators, drivers, sensors, and control hardware, and their integration with the flexure bearing.

Sensors and Drivers: A linear optical encoder (RELM scale, Si-HN-4000 Read-head, and SIGNUM Interface from Renishaw, 5nm resolution, 80mm range) was employed as the first X sensor between Ground and Stage 1. The resolution of a linear encoder is limited by its line grating period and electronic interpolation, and its digital output makes it immune to electronic noise. The encoder scale was mounted on Stage 1 while the encoder read-head is fixed to the ground, which allows easy routing of the read-head cable.

It was verified experimentally as well as analytically that the relative X displacement between Stage 1 and Motion Stage is of the order of tens of microns over the entire motion range of the system. Accordingly, a capacitance probe (Model # C23-C, Driver # CPL290 Elite Series from Lion Precision, 1nm resolution, 50μm range) was selected for the second X sensor. The probe was mounted on Stage 1 using a simple flexure-based clamp, while a high precision Starrett gauge block mounted on the Motion Stage served as the probe target.

The two sensor signals were fed to a real-time controller, where they are added in order to obtain the net X displacement of the Motion Stage w.r.t. Ground. An analogous arrangement was repeated along the Y direction.

Actuators and Drivers: Given the fixed-axis actuator integration capability provided by the proposed physical layout, several actuator options were considered. While PZT stack actuators may be integrated with suitable flexure based transmissions to amplify their motion range, this adversely affects the actuator stiffness and bandwidth at the transmission output. While inchworm-style quasi-static piezomotors are capable of the necessary range and resolution, their motion quality is compromised due to impact-induced vibrations even at low speeds [5]. Non-contact direct-drive electromagnetic linear motors are promising but often suffer from magnetic hysteresis and cogging. While cogging may be eliminated via slot-less and iron-less constructions [48], the single-phase non-commuted voice coil actuator (VCA) and moving magnet actuator (MMA) offer considerable simplicity in design and construction, along with non-contact cog-free motion, low cost, and sufficiently large stroke [49-51].

Although voice-coil actuators offer sufficiently large non-contact cog-free motion, their resolution, in practice, is limited by the Signal to Noise and Distortion Ratio (SINAD) or dynamic range of its current driver (or amplifier). SINAD includes both the broad-band Gaussian noise as well as harmonic distortion that may occur in an electronic circuitry [52]. A current driver provides direct control of the actuation force and offers a greater actuation bandwidth. A desired dynamic range of 10^7 or 140dB is extremely difficult, if not impossible, to achieve in practical high-current drivers due to the presence of broad-band noise and harmonic distortions. After considering several off-the-shelf current amplifiers, which proved to be inadequate, a custom built linear amplifier using an ultra-low noise power operational amplifier was designed to achieve a much improved SINAD of 90dB. Even though this still does not meet the desired dynamic range, the effect of amplifier noise on motion resolution could be subsequently mitigated via feedback control design. Based on this system-level solution for addressing the amplifier noise (partially via low-noise hardware and partially via feedback control), voice coils proved to be a promising actuator choice for large-range nanopositioning.

Based on the flexure bearing stiffness characteristics, voice coil actuators from BEI Kimco Magnetics (model LA24-20-000A) were selected for our application. These actuators have a force constant (K_{act}) of 11.12N/A and are capable of 111.2N bi-directional peak force. In the proposed physical layout (Fig. 3), since Stage 1 is constrained to move only along the X axis w.r.t. Ground, the actuator Mover may be directly attached to it. In fact, no additional bearing or decoupling is needed for the actuator, which provides considerable simplicity in the system integration. In our case, the permanent magnet of the voice-coil actuator is connected to Stage 1 as the Mover, while the coil is attached to the Ground frame as the Stator. This offers two advantages: first, a static coil avoids moving wires, which can

be a source of disturbance; and second, the coil, which is a heat source, is separated from the flexure bearing. The Ground frame with its greater thermal mass and surface area is better able to channel and dissipate this heat generated in the coil due to actuation current. In the future, we plan to carry out careful thermal modeling, and incorporate features in the detailed design that will effectively reject this heat and minimize its effect on the nanopositioning system performance.

The power OpAmp MP111 from Cirrus Logic MP111 was chosen for our custom-built current amplifier due to its high current capability and 10µV root-mean-square (RMS) output noise at 1MHz bandwidth. The servo amplifier was designed as an inverting voltage-controlled-current-source in a floating load configuration [53]. The gain (K_{amp}) and the bandwidth of the amplifier were set to be 1A/V and 1kHz, respectively. The bandwidth is set well above the frequency range of motion control. This amplifier was experimentally tested to show a broad-band Gaussian noise floor of –120dB and harmonic distortion of –90dB [32].

Real-time Control Hardware: The PXI-8106 real-time controller from National Instruments equipped with PXI-6289 data acquisition card was used to implement the closed-loop control algorithm. The sampling rate was fixed at 5kHz.

A video of the overall experimental hardware assembly and operation may be viewed at the authors' website [47].

5. DYNAMIC MODELING AND SYSTEM IDENTIFICATION

In this section, a dynamic model of the overall nanopositioning system is constructed and validated via experimental system identification, in preparation for control system design. In the frequency range of interest (~ 1-100Hz), the system may be modeled as a collection of lumped springs (DPFM) and masses (rigid stages). The DPFM is modeled here as a mass-less spring along both the axial and the transverse directions as shown in Fig. 4. The blue spring (solid line) represents the stiffness of the DPFM in its transverse direction and the red spring (dotted line) represents its stiffness in its axial direction. The mass of flexure beams and the secondary stage within the DPFM is neglected, in comparison to the mass of the rigid stages. Even though the stiffness of the DPFM in the in-plane yaw and out-of-plane directions is of the same order as the axial stiffness, these other motions are not included in this initial modeling attempt. It is recognized that in-plane rotational and out-of-plane modes will not be captured in the resulting dynamic model, but this assumption provides a degree of simplicity and still offers greater insight into the dynamics and controls of the proposed system.

One of the most important consequences of large deformations in flexure mechanisms is the variation of stiffness with loads and displacements. These stiffness variations have been extensively modeled for the DPFM in the past to yield the following closed-form parametric relations [46]:
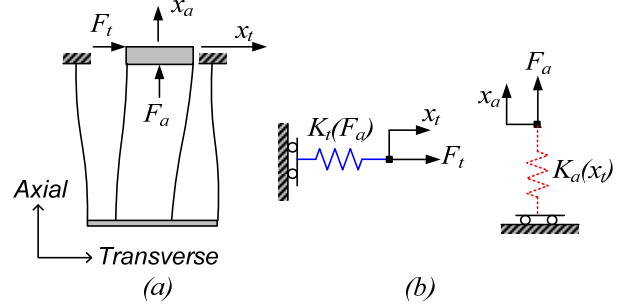

Fig.4 Lumped Spring Model of the Double Parallelogram Flexure Module along its Axial and Transverse Directions

$$K_t \approx \left[12 - \frac{3}{100}\left(\frac{F_a L^2}{EI} \right)^2 \right] \frac{EI}{L^3} \tag{1}$$

$$K_a \approx \frac{1}{\left(T^2 + \frac{9}{25} x_t^2 \right)} \cdot \frac{12EI}{L} \tag{2}$$

where E is the young's modulus of the material, and L, T and I denote the length, in-plane beam thickness, and second moment of area, respectively, of the constituent beams within the DPFM. The above relations indicate that the transverse direction stiffness of the DPFM drops quadratically with the axial force (F_a), and its axial direction stiffness has an inverse-quadratic dependence on the transverse displacement (x_t).

Assuming a geometric decoupling between the two axes, a 5-DoF lumped parameter X direction model for the proposed nanopositioning system is presented in Fig.5. The X displacements of the 5 rigid stages in the system define the five DoF. Stiffness variation in the X direction model due to Y direction force and displacement is incorporated in this model by means of the above stiffness relations. An analogous model may be constructed for the Y direction of the nanopositioning system. It is important to recognize that while there exists decoupling between the two axes in a geometric or kinematic sense, which avoids over-constraint and allows large motions, there does exist coupling in terms of stiffness parameters as indicated by the above analysis. This stiffness coupling is inevitable and affects the dynamic characteristics of nanopositioning system as seen below.

The actuator force acting on Stage 1 along the X direction represents the system input (u_x), and the displacement of the Motion Stage along the X direction is the output (x_{ms}). The governing equation of motion for the model shown in Fig. 5 can be written as follows:

$$[M]\{\ddot{x}\} + [C_d]\{\dot{x}\} + [K]\{x\} = \{f\}u_x \tag{3}$$

where $\{x\} = [x_1\ x_2\ x_3\ x_4\ x_{ms}]^T$ and $\{f\} = [1\ 0\ 0\ 0\ 0]^T$ are 5×1 displacement and force vectors, respectively. $[M]$, $[C_d]$, and $[K]$ are all 5×5 symmetric matrices representing mass, damping, and stiffness respectively. The mass and stiffness matrices in this model are as follows:
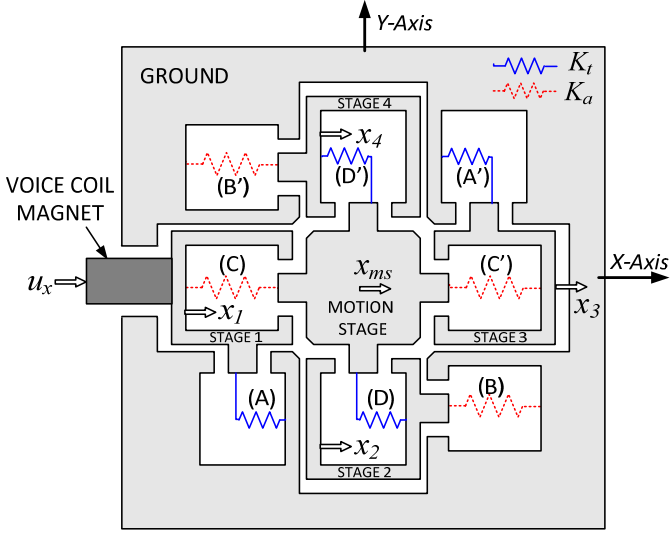
Fig. 5 5-DoF Spring-mass Model of the Nanopositioning System along the X Direction

$$[M] = \begin{bmatrix} M_{is} + M_{vc} & 0 & 0 & 0 & 0 \\ 0 & M_{is} & 0 & 0 & 0 \\ 0 & 0 & M_{is} & 0 & 0 \\ 0 & 0 & 0 & M_{is} & 0 \\ 0 & 0 & 0 & 0 & M_{ms} \end{bmatrix}$$

$$[K] = \qquad\qquad (4)$$

$$\begin{bmatrix} K_t^{(A)} + K_a^{(C)} & 0 & 0 & 0 & -K_a^{(C)} \\ 0 & K_t^{(D)} + K_a^{(B)} & 0 & 0 & -K_t^{(D)} \\ 0 & 0 & K_t^{(A')} + K_a^{(C')} & 0 & -K_a^{(C')} \\ 0 & 0 & 0 & K_t^{(D')} + K_a^{(B')} & -K_t^{(D')} \\ -K_a^{(C)} & -K_t^{(D)} & -K_a^{(C')} & -K_t^{(D')} & \left(\begin{matrix} K_t^{(D)} + K_a^{(C)} \\ +K_t^{(D')} + K_a^{(C')} \end{matrix} \right) \end{bmatrix}$$

where, $M_{is} = 0.177$Kg is the mass of Stages 1 through 4, $M_{vc} = 0.570$Kg is the mass of the voice coil mover and $M_{ms} = 0.284$Kg is the mass of the Motion Stage. In the stiffness matrix, $K_t^{(A)}$ represents the transverse stiffness of the DPFM (A), and so on. Here, the axial and transverse stiffness of all the DPFM are determined using Eqs.(1)-(2) for a given Y direction force or displacement.

To determine the analytical system transfer-function $G_{fx}(s) = X_{ms}(s)/U_x(s)$, a state-space model was derived using Eq.(3), with states $\{z_1\} = \{x\}$ and $\{z_2\} = \{\dot{x}\}$:

$$\begin{bmatrix} \dot{z_1} \\ \dot{z_2} \end{bmatrix} = \begin{bmatrix} 0 & I \\ -[M]^{-1}[K] & -[M]^{-1}[C_d] \end{bmatrix} \begin{bmatrix} z_1 \\ z_2 \end{bmatrix} + \begin{bmatrix} 0 \\ [M]^{-1} f \end{bmatrix} u_x$$

$$x_{ms} = \begin{bmatrix} 0 & 0 & 0 & 0 & 1 & 0 & 0 & 0 & 0 & 0 \end{bmatrix} \begin{bmatrix} z_1 \\ z_2 \end{bmatrix}$$

$$(5)$$

This analytical transfer function is plotted in Fig. 6a for the nominal X direction stiffness matrix $[K]$, with Y actuation set to zero. The first pole, which occurs at 18Hz, represents a rigid body mode in which Stage 1, Motion Stage, and stage 3 all move in phase with each other. The next higher mode of interest is at 1315Hz, where Motion Stage moves out of phase with respect to Stage 1, demonstrating the non-collocated sensing and actuation in our system. The corresponding pole falls outside the plotted frequency range, and is therefore not seen in Fig. 6a. A similar exercise may be carried out for non-zero Y actuation, which alters the X direction stiffness matrix $[K]$ as per Eqs.(1)-(2). The X direction transfer function for case of $y_{ms} = 5$mm is plotted in Fig. 6b. It is interesting to note that while there is no significant change in the rigid body mode, which remains at about 18Hz, the other mode mentioned above moves from down 1315Hz to about 150Hz.

The above dynamic response predicted by the 5-DOF X direction model is corroborated experimentally via broadband FFT-based identification techniques using a dynamic signal analyzer (SigLab, Model 20-22A). For system identification, the experimental set-up consists of the current amplifier, actuator, flexure bearing and the sensor. A band-limited chirp excitation was used within the frequency range of 1Hz to 500Hz. Since the actuator driver is operated in the current mode with a bandwidth of 1kHz, both the voice coil actuator and the current amplifier are approximated by constant gains ($K_{act} = 11.12$N/A, $K_{amp} = 1.0$A/V). This X direction system identification was carried out for y_{ms} values of 0 and 5mm, and the results (solid red line) are plotted in Fig. 6a and 6b, respectively. The $G_{fx}(s)$ transfer functions shown here are between the actuator force and Motion Stage displacement. Reasonably good agreement between the analytical prediction and experimental measurement is seen for both the Y actuation cases. Since damping was not incorporated in the analytical model, it was estimated based on the experimental response.

The critical difference between the transfer functions in Fig. 6a and 6b is observed at 150Hz, where the phase drops below 180° for the operating point in the latter case. Since the 5-DoF model incorporates the variation in X stiffness with Y actuation, it predicts the change in pole location, and thus the early phase loss, quite accurately. The experimental transfer functions show several additional modes, very likely arising from in-plane rotational and out-of-plane dynamics, which were not included in the 5-DoF model. However, despite its simplicity, this model captures all the essential dynamics that are pertinent to Motion Stage position control, up until 150Hz, throughout the operating range of motion.
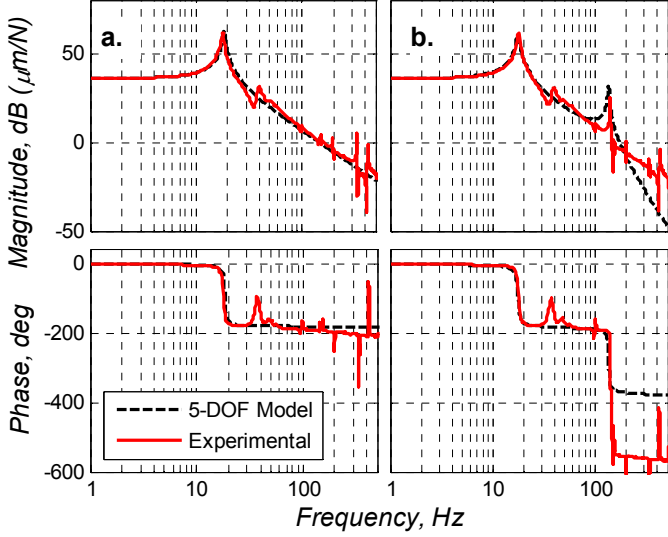
*Fig. 6 Comparison between Experimental and Analytical X Direction Frequency Response: (**a.**) $y_{ms} = 0$ and (**b.**) $y_{ms} = 5mm$*

6. CONTROL SYSTEM CHALLENGES AND DESIGN

In addition to motion range, the performance of a nanopositioning system is specified in terms of its motion precision, accuracy, and resolution, along with speed of operation. In a closed-loop setup, these specifications can be translated to equivalent control system design objectives. Accuracy and precision depend on command tracking as well as low frequency disturbance rejection. Positioning noise and the minimum incremental motion determine the resolution. While positioning noise depends on high frequency noise and disturbance rejection, minimum incremental motion is determined by command tracking. Closed-loop bandwidth determines the speed and response time of the nanopositioning system. Finally, closed-loop robustness against modeling uncertainties and parameter variations affect all of the above.

In the context of our physical system, several control design challenges and trade-offs were identified in achieving the above performance objectives:

1. Most existing nanopositioning systems have a high first natural frequency because they operate over a relatively small motion range. Therefore, simple lower-order integral controllers with loop crossover frequency less than the first resonance provide good overall performance [5]. In our case, the extended range of motion leads to low primary stiffness, resulting in a low first natural frequency (~ 18Hz). In order to achieve a bandwidth greater than this first natural frequency, a higher-order controller is needed, which poses greater performance trade-offs in terms of actuation effort, robustness, and noise and disturbance rejection.

2. In general, lightly damped poles and zeros of in a flexible system severely affect the closed loop stability and performance [54]. In addition to this, the non-collocation of sensor and the actuator in our case places additional limitations on the achievable bandwidth [55].

3. As mentioned in Section 5, the stiffness parameter variation results in variations in the frequency response along each axis over the operating motion range of the nanopositioning system. This plant variation poses challenges in obtaining robust stability and performance, especially at higher frequencies. Additionally, cross-axis coupling between the two axes, defined as the kinematic and/or elastic displacement along one axis due to actuation along the other axis, also degrades the positioning performance. This cross-axis coupling can be either linear or non-linear depending on its source.

4. Various sources of noise and disturbance in our system limit the positioning noise as well as command tracking. This includes feedback sensor noise, actuator driver noise and harmonic distortion, electronic noise in the data acquisition hardware, and mechanical floor vibrations. The individual contribution of these sources to the positioning noise depends upon their respective magnitude, where they enter the feedback system, the control architecture, and the controller design (Fig. 7).

In additional to these challenges that are specific to our physical system, any closed-loop framework, in general, is subject to fundamental limitations and trade-offs [56, 57]. One such trade-off pertinent in our case (between amplifier noise rejection and stability robustness) is discussed in further detail later in this section.

Having identified various control system objectives, challenges, and limitations, our goal in this paper is to attempt a preliminary control system design that can demonstrate large range nanopositioning capability at low speeds. Towards meeting this goal, we make two observations. One, while the effect of stiffness parameter variation on plant dynamics has been recognized in the modeling above, its effect is negligible in the low frequency range (< 150Hz), as seen in Fig. 6. Two, the cross-axis coupling between the two axes in this frequency range can be treated as an output disturbance from the perspective of each individual axis (Fig.7). Moreover, the harmonic distortion and noise in the current amplifier, which prove to be the biggest contributors to positioning noise and error, appear as input disturbance in the feedback control loop (Fig.7). Therefore, we propose to implement identical but
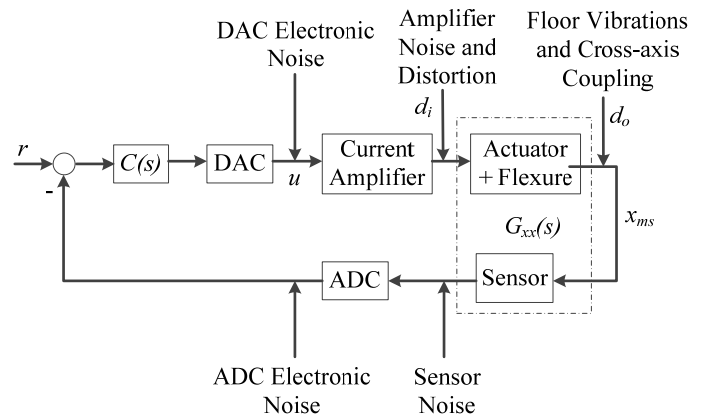

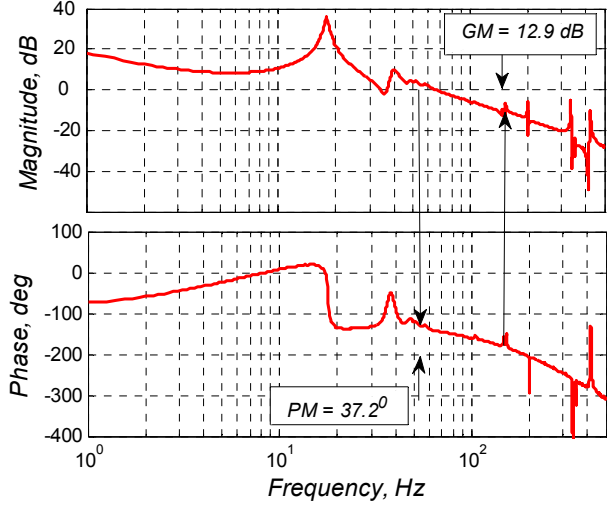*Fig.7 Control Architecture implemented along each axis*

Fig.8 Experimentally Measured Frequency Response of the Loop Transfer Function, L(s)
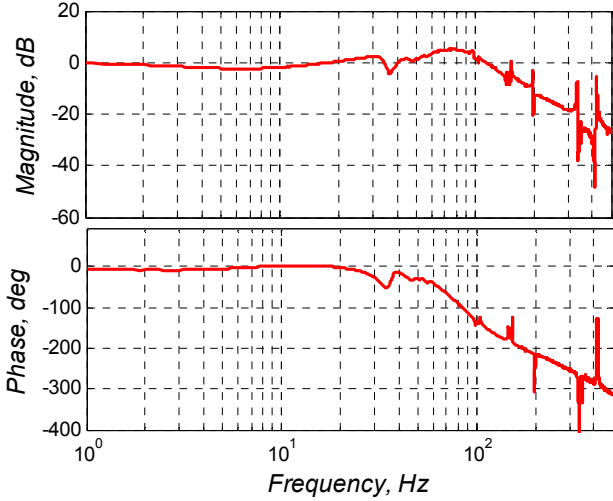

Fig. 9 Experimentally Measured Frequency Response of the Closed-loop Transfer Function
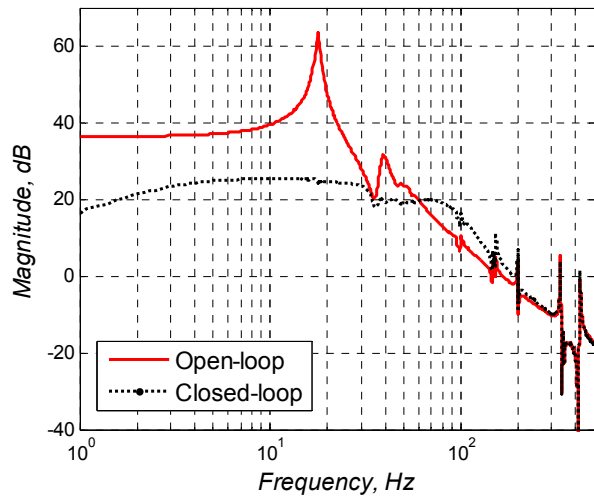

Fig. 10 Experimentally Measured Transfer Function from Amplifier Noise to Motion Stage Position

independent control schemes for each axis, with an emphasis on command tracking and disturbance rejection. As shown in Fig. 7, the voice coil actuator, the flexure bearing, and the sensor altogether are denoted by $G_{xx}(s)$, which is the same as $K_{act}*G_{fx}(s)$ assuming no sensor dynamics. The controller is represented by $C(s)$. The command is r, amplifier noise and distortion is d_i, ground vibration and cross-axis coupling is d_o, and the Motion Stage displacement is x_{ms}.

The transfer function derived from the 5-DOF model in Eq.(5) may be stated as follows:

$$G_{xx}(s) = 2.45 \times 10^{11} \frac{\left(s^2 + 7672s + 1.507 \times 10^7\right)}{\left(s^2 + 6.82s + 1.22 \times 10^4\right)} \times$$

$$\frac{1}{\left(s^2 + 24.05s + 7.12 \times 10^5\right)\left(s^2 + 5491s + 7.73 \times 10^6\right)} \quad (6)$$

This open-loop transfer function is used to design a lag-lead controller, $C(s)$, to achieve acceptable closed-loop stability and performance. The lag part includes an integrator to achieve zero steady state error and low frequency disturbance rejection and the lead part is needed to increase the phase near gain crossover frequency. In order to ensure a good roll-off at higher frequencies, an additional pole is added after the crossover frequency. After a few iterations, the following feedback controller was implemented:

$$C(s) = 170 \frac{(s+30)(s+71)}{s(s+1150)(s+2515)} \quad (7)$$

The experimentally measured frequency response of the resulting loop transfer function $L(s) = G_{xx}(s)C(s)$ along with corresponding stability margins is shown in Fig. 8. This confirms a Gain Margin (GM) or 12.9dB and a Phase Margin (PM) of 37.2°. Fig. 9 shows the experimentally obtained frequency response of the closed loop transfer functions from r to x_{ms}. The dip in gain and phase seen at lower frequencies is due to the zeros of the $C(s)$.

As mentioned earlier, from the perspective of each axis and its respective independent controller, the amplifier noise and distortion serve as input disturbance and the cross-axis coupling can be thought of as output disturbance. Therefore, it is important to consider the effect of the feedback controller in rejecting these disturbances. The closed-loop transfer functions from the input disturbance d_i and the output disturbance d_o to the Motion Stage displacement x_{ms} are given by:

$$T_{di-x}(s) = \frac{G_{xx}(s)}{1 + C(s)G_{xx}(s)}$$

$$T_{do-x}(s) = \frac{1}{1 + C(s)G_{xx}(s)} \quad (8)$$

It is clear that the ability of the closed-loop system to reject both the disturbances depends upon the magnitude of $C(s)$. In other words, higher closed-loop bandwidth, which requires a high $C(s)$ over a certain frequency range, ensures improved disturbance rejection. However, there is obviously a limit to
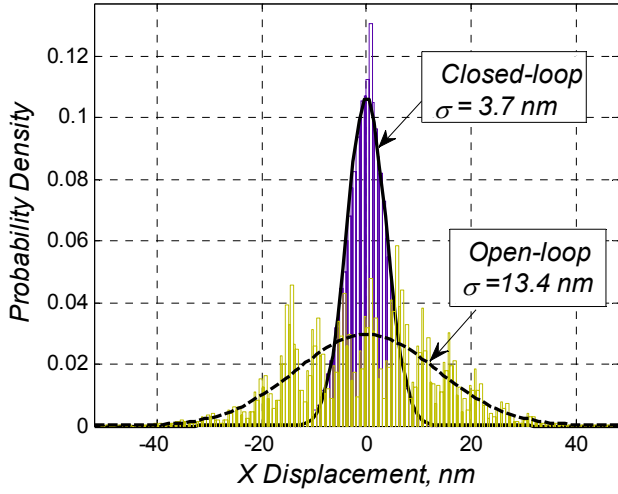
9

Fig. 11 Amplitude Distribution of the Open-loop and Closed-loop Positioning Noise

which $C(s)$ can be increased due to concerns arising from stability margins and sensor noise amplification [57]. For the controller $C(s)$ given in Eq.(7), Fig. 10 shows the comparison between the open-loop and closed-loop transfer functions $G_{xx}(s)$ and $T_{di-x}(s)$, from d_i to x. Thus, the improvement in input disturbance rejection is clearly evident. A similar trend exists for the output disturbance rejection.

7. PRELIMINARY RESULTS

In this section, we present some preliminary closed-loop performance plots for the proposed XY nanopositioning system based on the controller design discussed above. To measure the positioning noise, which is also representative of the resolution, the stage was commanded to stay at a fixed position. In the steady-state, the current amplifier harmonics and cross-axis coupling are absent and the current amplifier broad-band Gaussian noise is the dominant contributor to positioning noise. The effect of this input disturbance on x_{ms} is directly proportional to the area under the transfer function $T_{di-x}(s)$ in Fig.10 [10]. This area is approximately 4 times less than the area under the transfer function $G_{xx}(s)$, which indicates a corresponding improvement in disturbance rejection. Indeed, this is corroborated by the time domain analysis of positioning noise in Fig.11, which shows the probability density function of the open-loop and closed-loop positioning noise (x_{ms}). The closed-loop positioning noise is less than 4nm RMS, which is 3.6 times better than that measured in the open-loop.

Fig.12 shows the position response of the Motion Stage to step commands of size 1.5mm and 20nm (*inset*) along the X axis, over a 9mm range. The steady state positioning resolution as seen in this time-domain plot is under 4nm RMS, in agreement with Fig.11. Similar closed-loop positioning resolution, in point-to-point motion commands, was measured for the Y axis actuation, as well as simultaneous X and Y axis actuation. This figure (*inset*) also indicates a positioning

repeatability or precision of the order of the positioning resolution.

Next, the Motion Stage was commanded to move in a 5mm diameter circle at 1Hz. This was done by sending sinusoidal reference commands along both the axes with a magnitude of 2.5mm and separated in phase by 90°. The measured trajectory along with the ideal commanded circle is plotted in Fig. 13. For better visualization, the deviation from the ideal circle is magnified 25 times. The RMS of the radial error between the measured trajectory and the ideal circle is approximately 2.9μm. Corresponding RMS errors for the same diameter circle tracking at frequencies 0.1Hz and 0.01Hz were also measured and found to be 319nm and 58nm, respectively. A power spectrum analysis of these closed-loop tracking errors at various frequencies reveals the presence of three components: 1. magnitude and phase errors in the actual motion profile along
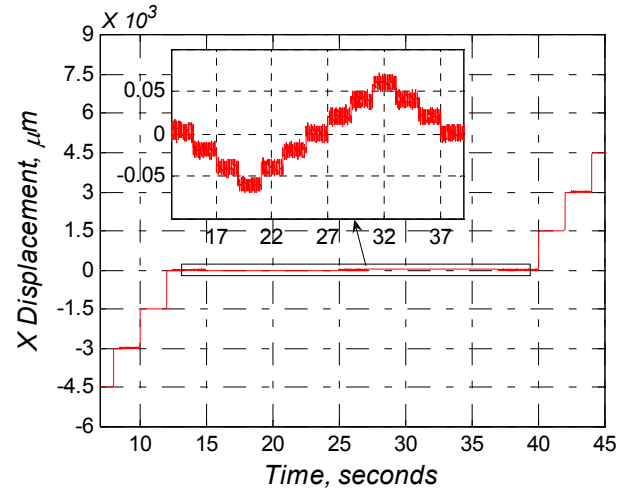

Fig. 12 Motion Stage Position Response for 1.5mm Steps and 20nm Steps Along X axis
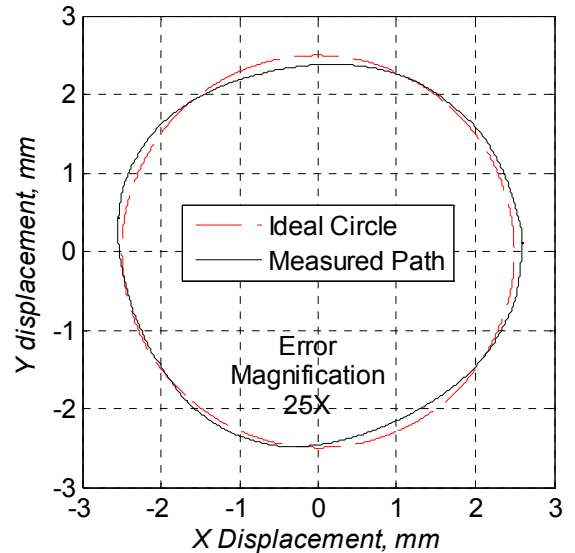

Fig. 13 Motion Stage Tracking a 5mm Diameter Circle

each axis with respect to the sine and cosine commands, 2. higher order harmonics of the commanded frequency, and 3. broad-band Gaussian noise.

The magnitude and phase error is due to lack of adequate closed-loop command following. The higher order harmonics in the measured trajectory arise from inadequate attenuation of the harmonic distortion in the current amplifier and the cross-axis coupling (i.e. input and output disturbance rejection). The broad-band positioning noise is largely due to the corresponding broad-band noise in the current amplifier. The circle tracking performance at lower frequencies is better, as noted above, due to relatively better command following and disturbance rejection provided by the feedback controller at these frequencies. However, achieving better command tracking and disturbance rejection at higher frequencies via linear feedback controllers results in tradeoffs with stability margins and sensor noise rejection, as explained in the previous section.

Thus, in the experimental results so far, large range and nanometric motion quality have been achieved in point-to-point positioning but not in dynamic command tracking.

8. CONCLUSION
We have presented a physical layout that holds the potential for achieving the goal of large-range XY nanopositioning. Meeting this objective has been a long-standing challenge because of the limitations posed by individual nanopositioning components as well as their integration, which have been identified and highlighted. A systematic constraint map has been employed to generate an XY parallel-kinematic physical system layout that ensures a high degree of geometric decoupling between the two motion axes, provides actuator isolation that allows the use of large-stroke single-axis actuators, and enables a complementary end-point sensing scheme that employs commonly available sensors.

The proposed physical system has been fabricated and assembled, and shown to be simultaneously capable of large range (10 mm per axis) and high motion quality, in principle, due to a lack of friction and backlash anywhere in the assembly. While preliminary closed-loop results provide a promising start, this exercise reveals the considerable challenges and trade-offs in the control system design. Even though the steady-state motion resolution and precision for point-to-point motion commands is in the desired range (4nm RMS), the dynamic command tracking error for a circular trajectory at 1 Hz is considerably large (2.9μm).

Our on-going research is aimed at achieving better tracking performance for dynamic commands. We plan to model the system as a Multi-Input Multi-Output (MIMO) system to capture the pertinent cross-axis coupling dynamics and design a MIMO controller accordingly. Furthermore, we are investigating iterative learning controls to reduce the periodic component of tracking error associated with higher order harmonics. Once these issues are addressed, we expect that the tracking error for dynamic commands can become comparable to that seen in point-to-point positioning. Thereafter, we will employ a 1nm resolution linear encoder (as opposed to 5nm resolution, at present) to target a motion quality approaching 1nm. Furthermore, we are also investigating the use of moving magnet actuators (MMA) instead of voice coil actuators (VCA). The former offers better thermal and dynamic performance because of fixed coils and smaller moving mass.

REFERENCES
[1] Hicks, T. R., and Atherton, P. D., 1997, *The Nanopositioning Book*, Queensgate Instruments Ltd.
[2] Sato, K., 2006, "Trend of Precision Positioning Technology," *ABCM symposium series in Mechatronics*, pp. 739-750.
[3] Jordan, S., and Lula, B., 2005, "*Nanopositioning: The Technology and the Options*," The 2005 Photonics Handbook.
[4] 2002, "*Application Note: Nanopositioning Tools and Techniques for R&D Applications*," nPoint Inc.
[5] Devasia, S., et al., 2007, "A Survey of Control Issues in Nanopositioning," *IEEE Transactions on Control Systems Technology*, 15(5), pp. 802-823.
[6] "*Product Model # NPS-XY-100A*," Queensgate Instruments.
[7] "*Product Model # P-541.2, Piezo XY Nanopositioning Stage*," Physik Instrumente.
[8] "*Product Model # NanoBio2200*," Mad City Labs.
[9] "*Product Model # PXY400*," PiezoSystem Jena.
[10] Aphale, S. S., et al., 2008, "Minimizing scanning errors in piezoelectric stack-actuated nanopositioning platforms," *IEEE Transactions on Nanotechnology*, 7(1), pp. 79-90.
[11] Dai, G., et al., 2004, "Metrological large range scanning probe microscope," *Rev Sci Instrum*, 75(4), pp. 962-969.
[12] Hausotte, T., et al., 2005, "Application of a Positioning and Measuring Machine for Metrological Long-range Scanning Force Microscopy," *SPIE*, pp. 1-12.
[13] Kramar, J. A., 2005, "Nanometre Resolution Metrology with the Molecular Measuring Machine," *Measurement Science & Technology*, 16(11), pp. 2121-2128.
[14] Sinno, A., et al., 2007, "Enlarged Atomic Force Microscopy Scanning Scope: Novel Sample-holder Device with Millimeter Range," *Rev Sci Instrum*, 78(9), pp. 1-7.
[15] Weckenmann, A., and Hoffmann, J., 2007, "Long Range 3 D Scanning Tunnelling Microscopy," *CIRP Annals - Manufacturing Technology*, 56(1), pp. 525-528.
[16] Salaita, K., et al., 2007, "Applications of Dip-Pen Nanolithography," *Nature Nanotechnology*, 2(3), pp. 145-155.
[17] Mirkin, C. A., 2001, "Dip-Pen Nanolithography: Automated Fabrication of Custom Multicomponent, Sub-100-Nanometer Surface Architectures," *MRS Bulletin*, 26(7), pp. 535-538.

[18] Sebastian, A., et al., 2008, "Nanopositioning for probe-based data storage [Applications of Control]," *IEEE Control Systems Magazine*, 28(4), pp. 26-35.

[19] Van de Moosdijk, M., et al., 2002, "Collinearity and stitching performance on an ASML stepper," *SPIE*, pp. 858-866.

[20] Hongzhong, L., et al., 2003, "A motor-piezo actuator for nano-scale positioning based on dual servo loop and nonlinearity compensation," *Journal of Micromechanics and Microengineering*, 13(2), pp. 295-299.

[21] Han, D., and Zhenhua, X., 2006, "*Motion stages for electronic packaging design and control*," IEEE Robotics & Automation Magazine, pp. 51-61.

[22] O'Brien, W., 2005, "*Long-range motion with nanometer precision*," Photonics Spectra, Laurin Publishing Co. Inc., Pittsfield, MA 01202-4949, United States, pp. 80-81.

[23] Fan, K.-C., et al., 2007, "Study of a noncontact type micro-CMM with arch-bridge and nanopositioning stages," *Robotics and Computer-Integrated Manufacturing*, 23(3), pp. 276-284.

[24] Maeda, G. J., and Sato, K., 2008, "Practical control method for ultra-precision positioning using a ballscrew mechanism," *Precision Engineering*, 32(4), pp. 309-318.

[25] Kim, W.-j., et al., 2007, "Design and precision construction of novel magnetic-levitation-based multi-axis nanoscale positioning systems," *Precision Engineering*, 31(4), pp. 337-350.

[26] Holmes, M., et al., 2000, "The long-range scanning stage: a novel platform for scanned-probe microscopy," *Precision Engineering*, 24(3), pp. 191-209.

[27] Maeda, G. J., et al., 2006, "Control of an XY nano-positioning table for a compact nano-machine tool," *JSME International Journal, Series C (Mechanical Systems, Machine Elements and Manufacturing)*, 49(1), pp. 21-27.

[28] Dejima, S., et al., 2005, "Dynamic modeling, controller design and experimental validation of a planar motion stage for precision positioning," *Precision Engineering*, 29(3), pp. 263-271.

[29] Culpepper, M. L., and Anderson, G., 2004, "Design of a low-cost nano-manipulator which utilizes a monolithic, spatial compliant mechanism," *Precision Engineering*, 28(4), pp. 469-482.

[30] Choi, Y.-M., et al., 2008, "Design and control of a nanoprecision XY Theta scanner," *Rev Sci Instrum*, 79(4), pp. 045109-045107.

[31] Pahk, H. J., et al., 2001, "Ultra precision positioning system for servo motor-piezo actuator using the dual servo loop and digital filter implementation," *International Journal of Machine Tools and Manufacture*, 41(1), pp. 51-63.

[32] Parmar, G., Hiemstra, D., Awtar, S., 2012, "Large Dynamic Range Nanopositioning Using Iterative Learning Control," *ASME Dynamic Systems and Control Conference*.

[33] Fischer, F. L., 1981, "*Symmetrical 3 DOF Compliance Structure*,"US.

[34] Smith, A. R., et al., 1994, "A new high resolution two-dimensional micropositioning device for scanning probe microscopy," *Rev Sci Instrum*, 64(10), pp. 3216-3219.

[35] Dagalakis, N. G., et al., 2001, "Kinematic Modelling and Analysis of Planer Micro-positioner," *ASPE 16th Annual Meeting*, pp. 135-138.

[36] Yao, Q., et al., 2007, "Design, analysis, fabrication and testing of a parallel-kinematic micropositioning XY stage," *International Journal of Machine Tools and Manufacture*, 47(6), pp. 946-961.

[37] Chen, K. S., et al., 2002, "Design and control for an electromagnetically driven X-Y-[theta] stage," *Precision Engineering*, 26(4), pp. 355-369.

[38] Awtar, S., 2004, "Analysis and Synthesis of Planer Kinematic XY Mechanisms," Sc.D., Massachusetts Institute of Technology, Cambridge MA.

[39] Awtar, S., and Slocum, A. H., 2005, "*Topology Evolution of High Performance XY Flexure Stages*," ASPE Annual MeetingNorfolk, VA.

[40] Zhelyaskov, V., et al., 2006, "*Automated piezoelectric nanopositioning systems - Long travel ranges and accurate angular movement create new opportunities in biomedical manipulation systems*," IEEE Circuits and Devices Magazine, Institute of Electrical and Electronics Engineers Inc., Piscataway, NJ 08855-1331, United States, pp. 75-78.

[41] Klocke, V., 2002, "Engineering in the nanocosmos: Nanorobotics moves kilograms of mass," *Journal of Nanoscience and Nanotechnology*, 2(3-4), pp. 435-440.

[42] Gao, W., et al., 2004, "A surface motor-driven planar motion stage integrated with an XY[theta]Z surface encoder for precision positioning," *Precision Engineering*, 28(3), pp. 329-337.

[43] "*Product # NanoGrid A Planar Encoder*," Optra Inc.

[44] "*Product # Series SP-D double plane-mirror interferometer*," SIOS Meßtechnik GmbH.

[45] Awtar, S., and Slocum, A. H., 2007, "Constraint-based Design of Parallel Kinematic XY Flexure Mechanisms," *ASME Journal of Mechanical Design*, 129(8), pp. 816-830.

[46] Awtar, S., et al., 2007, "Characteristics of Beam-based Flexure Modules," *ASME Journal of Mechanical Design*, 129(6), pp. 625-639.

[47] http://www.umich.edu/~awtar.

[48] Lee, M. G., et al., 2004, "Analysis of Halbach magnet array and its application to linear motor," *Mechatronics*, 14(Copyright 2004, IEE), pp. 115-128.

[49] Tat Joo, T., et al., 2008, "A flexure-based electromagnetic linear actuator," *Nanotechnology*, 19(31), pp. 1-10.

[50] Youm, W., et al., 2008, "Control of voice coil motor nanoscanners for an atomic force microscopy system using a loop shaping technique," *Rev Sci Instrum*, 79(1), pp. 013707-013706.

[51] Fukada, S., and Nishimura, K., 2007, "Nanometric positioning over a one-millimeter stroke using a flexure guide and electromagnetic linear motor," *International Journal of Precision Engineering and Manufacturing*, 8, pp. 49-53.

[52] Rapuano, S., et al., 2005, "ADC parameters and characteristics - Part 6 in a series of tutorials in instrumentation and measurement," *IEEE Instrumentation and Measurement Magazine*, 8(5), pp. 44-54.

[53] "*Application Note 13: Voltage to Current Conversion*," Cirrus Logic

[54] Book, W. J., 1993, "Controlled motion in an elastic world," *Transactions of the ASME. Journal of Dynamic Systems, Measurement and Control*, 115(2B), pp. 252-261.

[55] Spector, V. A., and Flashner, H., 1990, "Modeling and design implications of noncollocated control in flexible systems," *Transactions of the ASME. Journal of Dynamic Systems, Measurement and Control*, 112(2), pp. 186-193.

[56] Lee, C., and Salapaka, S. M., 2009, "Two degree of freedom control for nanopositioning systems: fundamental limitations, control design, and related trade-offs," *American Controls Conference*, pp. 1664-1669.

[57] Skogestad, S., and Postlethwaite, I., 2005, *Multivariable Feedback Control, Analysis and Design*, Wiley, New York.